examined here, there is a clear distinction between the short time or length scale of the microscopic theory and the long time or length scale of observables. As we show in (*15*), sloppiness in physics can be precisely traced to the ratio of these two scales—an important small variable. In the broad class of models in which such distinction of scales cannot be made, our explanation for sloppiness (*27*) is not yet unified with the RG and continuum methods of physics. Nonetheless, the striking similarity of their sloppy sensitivities lends perspective to the surprising power of mathematical modeling despite microscopic uncertainty.

References and Notes

1. E. P. Wigner, *Commun. Pure Appl. Math.* **13**, 1–14 (1960).
2. P. W. Anderson, *Science* **177**, 393–396 (1972).
3. U. Alon, *Nature* **446**, 497 (2007).
4. G. J. Stephens, B. Johnson-Kerner, W. Bialek, W. S. Ryu, *PLOS Comput. Biol.* **4**, e1000028 (2008).
5. G. J. Stephens, L. C. Osborne, W. Bialek, *Proc. Natl. Acad. Sci. U.S.A.* **108**, 15565–15571 (2011).
6. T. D. Sanger, *J. Neurosci.* **20**, 1066–1072 (2000).
7. F. Corson, E. D. Siggia, *Proc. Natl. Acad. Sci. U.S.A.* **109**, 5568–5575 (2012).
8. M. Schmidt, H. Lipson, *Science* **324**, 81–85 (2009).
9. T. Mora, W. Bialek, *J. Stat. Phys.* **144**, 268–302 (2011).
10. K. S. Brown *et al.*, *Phys. Biol.* **1**, 184–195 (2004).
11. R. N. Gutenkunst *et al.*, *PLOS Comput. Biol.* **3**, 1871–1878 (2007).
12. J. J. Waterfall *et al.*, *Phys. Rev. Lett.* **97**, 150601 (2006).
13. M. K. Transtrum, B. B. Machta, J. P. Sethna, *Phys. Rev. Lett.* **104**, 060201 (2010).
14. M. K. Transtrum, B. B. Machta, J. P. Sethna, *Phys. Rev. E Stat. Nonlin. Soft Matter Phys.* **83**, 036701 (2011).
15. Materials and methods are available as supplementary materials on *Science* Online.
16. S. Amari, H. Nagaoka, *Methods of Information Geometry* (American Mathematical Society, Providence, RI, 2000).
17. I. J. Myung, V. Balasubramanian, M. A. Pitt, *Proc. Natl. Acad. Sci. U.S.A.* **97**, 11170–11175 (2000).
18. V. Balasubramanian, *Neural Comput.* **9**, 349–368 (1997).
19. P. M. Chaikin, T. C. Lubensky, *Principles of Condensed Matter Physics* (Cambridge Univ. Press, Cambridge, 1995).
20. S. L. Veatch, O. Soubias, S. L. Keller, K. Gawrisch, *Proc. Natl. Acad. Sci. U.S.A.* **104**, 17650–17655 (2007).
21. G. E. Crooks, *Phys. Rev. Lett.* **99**, 100602 (2007).
22. J. Cardy, *Scaling and Renormalization in Statistical Physics* (Cambridge Univ. Press, Cambridge, 1996).
23. G. Ruppeiner, *Rev. Mod. Phys.* **67**, 605–659 (1995).
24. D. Ron, R. H. Swendsen, A. Brandt, *Phys. Rev. Lett.* **89**, 275701 (2002).
25. F. P. Casey *et al.*, *IET Syst. Biol.* **1**, 190–202 (2007).
26. J. F. Apgar, D. K. Witmer, F. M. White, B. Tidor, *Mol. Biosyst.* **6**, 1890–1900 (2010).
27. In (*13*, *14*), we used interpolation theorems and information geometry to show that multiparameter models fit to collective data have model manifolds that form hyper-ribbons in data space with geometrically spaced widths.

Acknowledgements: We thank S. Kuehn and S. Papanikolaou for helpful comments and discussions. This work was supported by NSF grants DMR 1005479 and DMR 1312160 and a Lewis-Sigler Fellowhip (B.B.M.). Raw data and analysis code are available on request from the authors or via the Internet: www.lassp.cornell.edu/sethna/Sloppy/EmergentParameterCompression.

Supplementary Materials

www.sciencemag.org/content/342/6158/604/suppl/DC1
Supplementary Text
Figs. S1 and S2
References (*28*–*42*)

4 April 2013; accepted 24 September 2013
10.1126/science.1238723

Deterministically Encoding Quantum Information Using 100-Photon Schrödinger Cat States

Brian Vlastakis,[1]* Gerhard Kirchmair,[1]† Zaki Leghtas,[1,2] Simon E. Nigg,[1]‡ Luigi Frunzio,[1] S. M. Girvin,[1] Mazyar Mirrahimi,[1,2] M. H. Devoret,[1] R. J. Schoelkopf[1]

In contrast to a single quantum bit, an oscillator can store multiple excitations and coherences provided one has the ability to generate and manipulate complex multiphoton states. We demonstrate multiphoton control by using a superconducting transmon qubit coupled to a waveguide cavity resonator with a highly ideal off-resonant coupling. This dispersive interaction is much greater than decoherence rates and higher-order nonlinearities to allow simultaneous manipulation of hundreds of photons. With a tool set of conditional qubit-photon logic, we mapped an arbitrary qubit state to a superposition of coherent states, known as a "cat state." We created cat states as large as 111 photons and extended this protocol to create superpositions of up to four coherent states. This control creates a powerful interface between discrete and continuous variable quantum computation and could enable applications in metrology and quantum information processing.

Cavity quantum electrodynamics is a testbed system for quantum optics, allowing the observation of strong interactions between photons and (artificial) atoms (*1*–*3*). Techniques using these systems allow the production of nonclassical states of light, which have important uses for quantum communication, quantum computation, and investigations of fundamental quantum theory. For superconducting quantum circuits, cavity resonators have proven a valuable resource serving several roles: a quantum bus to generate entanglement between qubits (*4*), a quantum nondemolition probe allowing efficient quantum measurements (*5*, *6*), a generator of single microwave photons (*7*, *8*), and a quantum memory to store and shuttle information (*9*, *10*). With its large Hilbert space, a cavity resonator also has the potential to store multiple quantum bits or redundantly encode information as necessary for quantum error correction. With the proper controls, a single cavity could be made equivalent to a multiqubit register, allowing for simplifications of hardware design (*11*, *12*). Although there have been some investigations of complex, multiphoton superpositions in superconducting cavity resonators, most techniques developed so far require fast qubit frequency tunability and are based on controlling individual photons one by one (*13*, *14*). These implementations become increasingly burdensome for complex states or large photon numbers, making it desirable to develop a more natural method for controlling the large cavity Hilbert space.

We demonstrated a set of multiphoton operations by using a fixed-frequency superconducting transmon qubit coupled to a waveguide cavity resonator. We realized a highly ideal strong-dispersive coupling, where the strengths of the off-resonant qubit-cavity interactions were several orders of magnitude greater than the cavity decay rate and higher-order nonlinearities. This created a set of qubit-cavity entangling operations, allowing for control over the large cavity phase space. We implemented two of these operations: the qubit-state conditional cavity phase shift (*15*) and the photon-number conditional qubit rotation (*14*, *16*). We combined these with unconditional qubit and cavity operations to perform direct measurements of the cavity Wigner function (*17*) and to efficiently generate large superposition states. By using these tools, we realized a recently proposed protocol (*18*) to deterministically encode quantum information in a cat state by creating an arbitrary superposition of quasi-orthogonal coherent states conditioned on an initial qubit state. We concatenated these entangling operations to encode quantum information into multiple phases of the cavity state, thereby creating multicomponent cat states and producing example states

[1]Department of Physics and Department of Applied Physics, Yale University, New Haven, CT 06511, USA. [2]Inria Paris-Rocquencourt, 78153 Le Chesnay Cedex, France.

*Corresponding author. E-mail: brian.vlastakis@yale.edu
†Present address: Institut für Quantenoptik und Quanteninformation, Österreichische Akademie der Wissenschaften, Otto-Hittmair-Platz 1, A-6020 Innsbruck, Austria, and Institut für Experimentalphysik, Universität Innsbruck, Technikerstrasse 25, A-6020 Innsbruck, Austria.
‡Present address: Department of Physics, University of Basel, CH-4056 Basel, Switzerland.

proposed for high-precision measurements surpassing the quantum-noise limit (*19*, *20*). Unlike previous demonstrations of cat states (*16*, *21*, *22*), the procedures realized here allow for the deterministic generation of superimposed coherent states with arbitrary phase and amplitude. The set of operations demonstrated provides an efficient method to manipulate coherent states and could enable a variety of powerful methods for using cavity states in quantum information processing.

We realized qubit-photon quantum logic by using a strong off-resonant coupling of a qubit and cavity that can be described by the dispersive Hamiltonian (omitting higher-order nonlinear terms)

$$H/\hbar = \omega_q|e\rangle\langle e| + \omega_s a^\dagger a - \chi_{qs} a^\dagger a|e\rangle\langle e| \quad (1)$$

where $|e\rangle$ is the excited state of the qubit, $a^\dagger(a)$ are the raising (lowering) ladder operators of the cavity resonator, $\omega_{q,s}$ are qubit and cavity transition frequencies, and χ_{qs} is the dispersive interaction between these modes. This interaction produces a state-dependent shift in either the qubit or cavity transition frequency. We exploited this conditional frequency shift to produce qubit-photon entanglement with two operations: conditional cavity phase shifts and conditional qubit rotations. The conditional cavity phase shift can be described as

$$C_\Phi = e^{i\Phi a^\dagger a|e\rangle\langle e|} = \mathbb{1} \otimes |g\rangle\langle g| + e^{i\Phi a^\dagger a} \otimes |e\rangle\langle e| \quad (2)$$

where $|g\rangle$ is the ground state of the qubit and Φ is the conditional phase shift induced on the cavity state. This conditional phase appears from the free evolution of the dispersive Hamiltonian for a time τ where $\Phi = \chi_{qs}\tau$. For example, acting a conditional cavity phase shift on a coherent state while the qubit is in a superposition state produces an entangled qubit/cavity state, $C_\Phi\{|\alpha\rangle \otimes (|g\rangle + |e\rangle)\} = |\alpha, g\rangle + |\alpha e^{i\Phi}, e\rangle$ (disregarding normalization) (*15*). Because a coherent state $|\alpha\rangle = e^{-\frac{|\alpha|^2}{2}} \sum_{n=0}^{\infty} \frac{\alpha^n}{\sqrt{n!}} |n\rangle$ is a superposition of Fock states $|n\rangle$ represented by a complex value α, this operation enables us to encode the qubit state information into the cavity phase and entangle the qubit with many photons simultaneously. For a special case, $C_{\Phi=\pi}$, the cavity state attains a conditional π shift per photon. This, in turn, causes the qubit state to acquire a phase shift conditional on there being exactly an odd number of photons in the cavity, resulting in a mapping of the cavity photon number parity to the qubit state. By using Ramsey interferometry, we used this gate to measure the cavity photon parity and ultimately the cavity Wigner function (*17*, *23*, *24*). The Wigner function is a representation of a quantum state in a continuous variable basis and can be expressed as $W(\alpha) = \frac{2}{\pi} \mathrm{Tr}[D_\alpha^\dagger \rho D_\alpha P]$, where $D_\alpha = e^{\alpha a^\dagger - \alpha^* a}$ is the cavity displacement operator, $P = e^{i\pi a^\dagger a}$ is the photon number parity operator, and ρ is the cavity state density matrix. A direct Wigner measurement is produced by measuring the mean photon parity $\langle P \rangle$ at many points in the cavity phase space, which we used to completely determine the quantum state of the cavity.

The second operation, the conditional qubit rotation, is a rotation on the qubit state conditional on the photon number of the cavity state. Because the qubit transition frequency is strongly photon number dependent, we can drive a particular transition selective on a cavity Fock state (*14*, *16*). A rotation on the qubit state conditioned on the mth photon Fock state can ideally be described as

$$R^m_{\hat{n},\theta} = |m\rangle\langle m| \otimes R_{\hat{n},\theta} + \sum_{n \neq m} |n\rangle\langle n| \otimes \mathbb{1} \quad (3)$$

where $R_{\hat{n},\theta}$ is a qubit rotation about a vector $\hat{n}$ with rotation angle θ. In practice, this operation will result in residual photon-dependent phase shifts because of the ac Stark effect, which we corrected for the purposes of this experiment (*24*). In order to realize these two entangling operations, we had to achieve dispersive shifts much greater than the qubit and cavity decoherence rates, $\chi_{qs} \gg \gamma, n_{max}\kappa_s$, where γ is the qubit decay rate, κ_s is the storage cavity decay rate, and n_{max} is the maximum occupied photon number. This dispersive approximation (Eq. 1) is valid in a low photon number regime where the dispersive interaction $\chi_{qs} a^\dagger a|e\rangle\langle e|$ is much greater than higher-order nonlinear terms, such as the cavity self-Kerr $K_s a^{\dagger 2} a^2$, and the nonlinearity of the dispersive shift $\chi'_{qs} a^{\dagger 2} a^2 |e\rangle\langle e|$ (*25*). Combined with unconditional qubit and cavity manipulations, these two entangling operations give us a powerful tool set for controlling the joint qubit-cavity system (*12*, *18*, *24*).

Our experiment consists of two waveguide cavity resonators (*16*, *26*) coupled to a transmon qubit (Fig. 1A). Cavity 1 was used for photon-state manipulation, preparation, and storage with transition frequency $\frac{\omega_s}{2\pi} = 8.18$ GHz and decay rate $\frac{\kappa_s}{2\pi} = 7.2$ kHz $= \frac{1}{2\pi \times 22.1\,\mu s}$ (limited by internal losses). Cavity 2 was used for qubit-state detection with transition frequency $\frac{\omega_r}{2\pi} = 9.36$ GHz and decay rate $\frac{\kappa_r}{2\pi} = 330$ kHz $= \frac{1}{2\pi \times 480\mathrm{ns}}$ (limited by output coupling for increased readout fidelity). Both cavities were coupled to a "vertical" transmon qubit (*16*, *24*) with transition frequency $\frac{\omega_q}{2\pi} = 7.46$ GHz and decay rate $\frac{\gamma}{2\pi} = 36$ kHz $= \frac{1}{2\pi \times 4.4\,\mu s}$ (limited by internal losses). This system creates a dispersive interaction between the qubit and storage cavity mode, resulting in a state-dependent frequency shift $\frac{\chi_{qs}}{2\pi} = 2.4$ MHz. We independently measured (*24*) higher-order nonlinear terms K_s and χ'_{qs}, allowing us to put a limit on the maximum accessible photon number for this experiment: $n \ll n_{max} = \min[\chi_{qs}/\chi'_{qs} = 560, \chi_{qs}/K_s = 650, \chi_{qs}/\kappa_s = 330]$. By combining a conditional cavity phase shift with a conditional qubit rotation, we sequentially entangled then disentangled the qubit and cavity to map a qubit state to a superposition of quasi-orthogonal coherent states (*18*). Following the sequence outlined in Fig. 1B, we started with an unentangled qubit-cavity state $|\psi_0\rangle = |\beta\rangle \otimes (|g\rangle + |e\rangle)$ (disregarding normalization), where $|\beta\rangle$ is a coherent state. Performing a conditional cavity π phase shift on the initialized state created an entangled qubit-cavity state $|\psi_1\rangle = C_\pi|\psi_0\rangle = |\beta, g\rangle + |-\beta, e\rangle$. This state, where the qubit state is entangled with the phases of the superimposed coherent states, is often referred

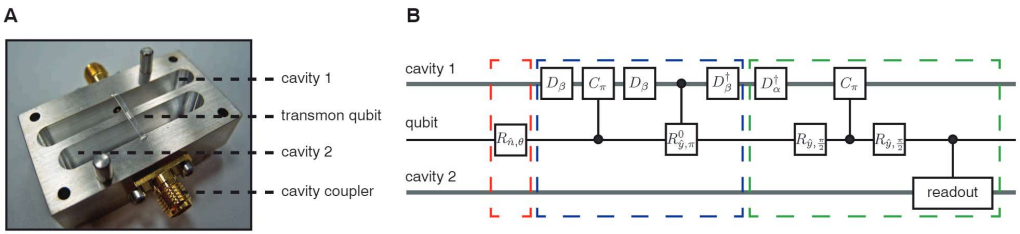

Fig. 1. Experimental device and protocol. (**A**) A cross section shows the device, machined from two halves of aluminum alloy, which contains two cavity resonators and holds a sapphire chip with a lithographically patterned transmon qubit. (**B**) The protocol for mapping and measuring a qubit state into a superposition of coherent states is performed in three steps: qubit-state preparation (red) using a single qubit rotation $R_{\hat{n},\theta}$; qubit to cavity-state mapping (blue) using conditional operations C_π and $R^0_{\hat{y},\pi}$ with cavity displacements D_β; and cavity-state Wigner tomography (green) using Ramsey interferometry with unconditional qubit rotations $R_{\hat{y},\frac{\pi}{2}}$.

to as a Schrödinger cat, which has been studied in other quantum systems (*15*, *27*). We can unconditionally displace this state to obtain $|\psi_2\rangle = D_\beta|\psi_1\rangle = |2\beta,g\rangle + |0,e\rangle$. At this point, we can apply a qubit π rotation conditional on the cavity vacuum state $|0\rangle$, which produces the unentangled cat state $|\psi_3\rangle \approx R^0_{\hat{y},\pi}|\psi_2\rangle = (|2\beta\rangle + |0\rangle) \otimes |g\rangle$. Because of the nonorthogonality of coherent states, this operation will leave some remaining entanglement, which rapidly decreases with cat state size and can be neglected compared with other experimental imperfections. An additional displacement results in the final state $|\psi_4\rangle = D_{-\beta}|\psi_3\rangle = (|\beta\rangle + |-\beta\rangle) \otimes |g\rangle$. As an example, we created the target cavity state $|\psi_{targ}\rangle = \mathcal{N}(|\beta\rangle + |-\beta\rangle)$, where $\mathcal{N} \approx \frac{1}{\sqrt{2}}$ with $|\beta| = \sqrt{7}$, resulting in a fidelity $F = \langle\psi_{targ}|\rho|\psi_{targ}\rangle = 0.81$, which we confirmed by direct Wigner tomography (Fig. 2A). This procedure can be generalized to any arbitrary qubit state and cavity phase that maps as

$$|0\rangle \otimes \{\cos\left(\frac{\theta}{2}\right)|g\rangle + \sin\left(\frac{\theta}{2}\right)e^{i\phi}|e\rangle\} \rightarrow$$

$$\{\cos\left(\frac{\theta}{2}\right)|\beta\rangle + \sin\left(\frac{\theta}{2}\right)e^{i\phi}|\beta e^{i\Phi}\rangle\} \otimes |g\rangle \quad (4)$$

where θ and ϕ are parameters of the initial qubit state and when the superimposed coherent states are sufficiently orthogonal $|\langle\beta|\beta^{i\Phi}\rangle|^2 \ll 1$. Figure 2B shows the creation of cat states conditioned by qubit states prepared at the six cardinal points of the Bloch sphere.

Two special forms of cat states result in complete destructive interference of either odd or even Fock state amplitudes. Known as the even (or odd) cat states $|\beta\rangle \pm |-\beta\rangle$, these states produce superpositions of only even (or odd) photon numbers. This interference can be showcased in the dispersive regime by performing qubit spectroscopy after the creation of one of these cavity states. Because of the strong-dispersive interaction, each spectral peak reveals a photon number probability of the prepared cavity state (*28*). For a coherent state $|\beta\rangle$, the qubit spectrum will represent a Poissonian photon number distribution $P_n(|\beta\rangle) = |\langle n|\beta\rangle|^2 = \frac{e^{-|\beta|^2}|\beta|^{2n}}{n!}$. An even and odd cat state of equivalent amplitude follows this same envelope but with destructive interference for the odd and even photon number states, respectively, $P_n(|\beta\rangle \pm |-\beta\rangle) \approx (1 \pm e^{i\pi n})\frac{e^{-|\beta|^2}|\beta|^{2n}}{n!}$. We perform spectroscopy on the qubit with three prepared states: $|\beta, g\rangle$, $\{|\beta\rangle + |-\beta\rangle\} \otimes |g\rangle$, and $\{|\beta\rangle - |-\beta\rangle\} \otimes |g\rangle$ for $|\beta| = 2.3$, illustrating the discreteness of the electromagnetic signals in the cavity and revealing the nonclassical nature of the generated cat states (Fig. 3A).

Unlike building photon superpositions one by one (*13*, *14*), this mapping protocol can scale to cavity states with larger quantum superpositions by merely increasing the displacement amplitude. The size of a quantum superposition in a cat state $S = |\beta_1 - \beta_2|^2$ is determined by its square distance in phase space between the two superimposed coherent states, $|\beta_1\rangle$ and $|\beta_2\rangle$ (*21*). To characterize S without performing full state tomography, we measured cuts of the Wigner function along the axis perpendicular to its quantum interference, W [Re(α) = 0, Im(α)]. The interference fringes in these cuts appear as $W[0,\mathrm{Im}(\alpha)] = Ae^{-2|\mathrm{Im}(\alpha)|^2}\cos[2\sqrt{S}\ \mathrm{Im}(\alpha) + \delta]$, where A and δ are the fringe amplitude and phase (*29*). By using this method, we created and confirmed cat states with sizes from 18 to 111 photons (Fig. 3B). The increased oscillation rate of these fringes with S shows the increased sensitivity to small displacements in cavity field because of larger quantum superpositions [see (*24*) for proof-of-principle Heisenberg-limited phase estimation]. Reduced fringe visibility with larger sizes is due to the increased sensitivity to cavity decay. Other factors also contribute, namely, infidelity in Wigner tomography and qubit decoherence during preparation.

Because the methods outlined here are deterministic, entangling operations can be combined to create complex nonclassical cavity states. By using a conditional cavity phase shift for various phases Φ, we can encode quantum information to a particular phase of a coherent state. With this operation, we can create superpositions of multiple coherent states, multicomponent cat states. We used gates $C_{2\pi/3}$ and $C_{\pi/2}$ to create three- and four-component cat states (Fig. 4, A to C) with fidelity $F_A = 0.60$, $F_B = 0.58$, and $F_C = 0.52$ (*24*). The skewing of these states is caused by the inherited cavity self-Kerr. Additional factors contributing to infidelity include photon decay during preparation and measurement as well as tomography pulse errors. The state in Fig. 4C, also known as the compass state, contains overlapping interference fringes revealing increased sensitivity to cavity displacements in both quadratures simultaneously (*19*).

We have demonstrated the efficient generation and detection of coherent state superpositions using off-resonant interactions inherent in the cavity QED architecture. The tools and techniques described here require only a fixed-frequency, strong-dispersive interaction and realize an inter-

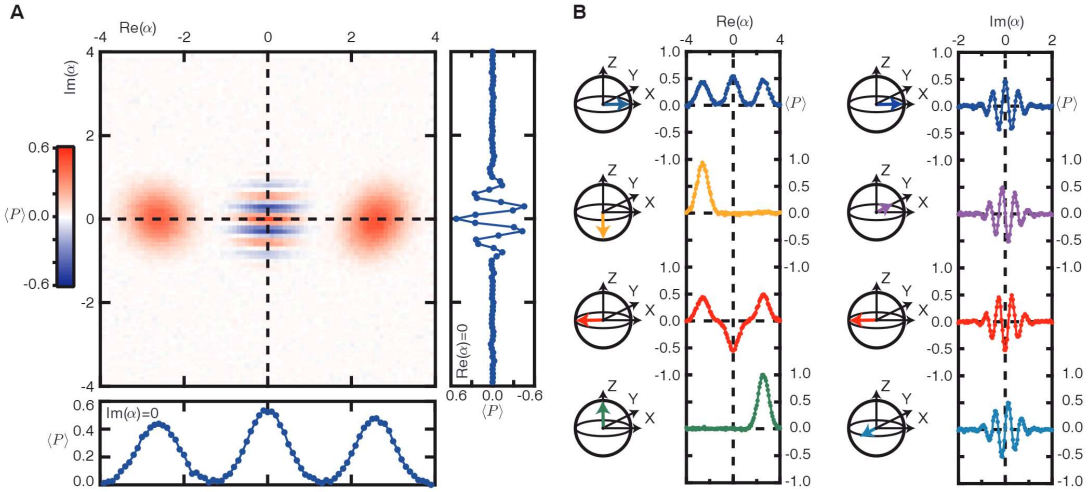

Fig. 2. Wigner tomography of coherent state superpositions. (A) Wigner tomography of the cavity state $|\psi\rangle = \mathcal{N}(|\beta\rangle + |-\beta\rangle)$ with $|\beta| = \sqrt{7}$ and $\mathcal{N} \approx \frac{1}{\sqrt{2}}$ using an 81-by-81 grid of tomography displacements showcases the interference fringes characteristic of a quantum superposition. Cuts along the real and imaginary axes reveal the relative population and quantum interference of the superimposed coherent states. The visibility of these interference fringes is reduced because of cavity decay during preparation and measurement (a perfect superposition would achieve unity mean photon parity). **(B)** By using qubit states initially prepared in the six cardinal points of the Bloch sphere, we mapped populations and phases in a resulting cat state.

face between discrete and continuous variable quantum computation (*30*). This can lead to simplified methods for individual storage and retrieval of multiqubit states in a cavity resonator and creates ways to perform multiqubit stabilizer measurements (*31*) or to redundantly encode information for quantum error correction (*12*) using minimal hardware. Additional applications include Heisenberg-limited measurement (*19*, *20*, *24*) and quantum information storage in thermally excited resonator states (*32*).

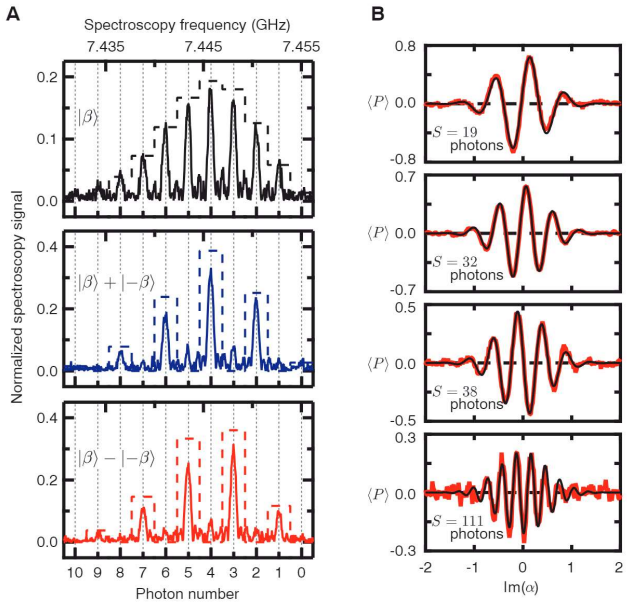

Fig. 3. Qubit spectroscopy and scaling to large photon superpositions. (**A**) Photon number splitting is observed when performing spectroscopy of a qubit dispersively coupled to the storage cavity with three different prepared states: a coherent state $|\beta\rangle$, even cat state $|\beta\rangle + |-\beta\rangle$, and odd cat state $|\beta\rangle - |-\beta\rangle$ with amplitude $|\beta| = 2.3$. Each spectral peak corresponds to the probability for a photon number state following a Poissonian distribution. Dashed bar plots show the expected photon probabilities for each of these states. Notice that even and odd cat states show destructive interference for the odd and even photon numbers. These spectra are acquired by deconvolving the measured signal with the Fourier spectrum of the finite-width spectroscopy pulse. (**B**) Cuts along the imaginary axis of the measured Wigner function for each prepared cat state reveal quantum superpositions with up to 111 photons in size. Cat state size S is determined by these measured interference fringes following the relation $Ae^{-2|\mathrm{Im}(\alpha)|^2}\cos[2\sqrt{S}\,\mathrm{Im}(\alpha) + \delta]$, where S, A, and δ are fit parameters.

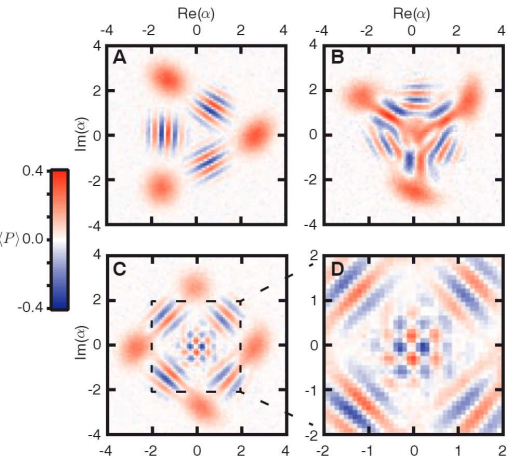

Fig. 4. Multicomponent cat states. By using conditional cavity phase shifts $C_{2\pi/3}$ and $C_{\pi/2}$, we created superpositions of three and four coherent states. Shown here is Wigner tomography of cavity states: (**A**) $|\beta\rangle + e^{i\lambda_1}|\beta e^{i2\pi/3}\rangle + e^{i\lambda_2}|\beta e^{i4\pi/3}$, where $|\beta| = \sqrt{7}$, $\lambda_1 = 0.6\pi$, and $\lambda_2 = -0.3\pi$; (**B**) $|0\rangle + e^{i\mu_1}|-i\beta\rangle + e^{i\mu_2}|\beta e^{i\pi/3}\rangle + e^{i\mu_3}|\beta e^{i2\pi/3}\rangle$, where $|\beta| = \sqrt{7}$, $\mu_1 = 0.5\pi$, $\mu_2 = -0.4\pi$, and $\mu_3 = -0.2\pi$; and (**C**) $|\beta\rangle + e^{i\nu_1}|i\beta\rangle + |-\beta\rangle + e^{i\nu_2}|-i\beta\rangle$, where $|\beta| = \sqrt{7}$, $\nu_1 = \pi$, and $\nu_2 = -0.2\pi$. (**D**) A closer inspection of the quantum interference in (**C**) reveals increased sensitivity to cavity displacements in both quadratures simultaneously.

References and Notes

1. J. M. Raimond *et al.*, *J. Phys. B* **38**, S535–S550 (2005).
2. R. Miller *et al.*, *J. Phys. B* **38**, S551–S565 (2005).
3. A. Wallraff *et al.*, *Nature* **431**, 162–167 (2004).
4. L. DiCarlo *et al.*, *Nature* **460**, 240–244 (2009).
5. R. Vijay, D. H. Slichter, I. Siddiqi, *Phys. Rev. Lett.* **106**, 110502 (2011).
6. M. Hatridge *et al.*, *Science* **339**, 178–181 (2013).
7. A. A. Houck *et al.*, *Nature* **449**, 328–331 (2007).
8. C. Eichler *et al.*, *Phys. Rev. Lett.* **109**, 240501 (2012).
9. P. J. Leek *et al.*, *Phys. Rev. Lett.* **104**, 100504 (2010).
10. M. Mariantoni *et al.*, *Nat. Phys.* **7**, 287–293 (2011).
11. D. Gottesman, A. Kitaev, J. Preskill, *Phys. Rev. A* **64**, 012310 (2001).
12. Z. Leghtas *et al.*, *Phys. Rev. Lett.* **111**, 120501 (2013).
13. M. Hofheinz *et al.*, *Nature* **459**, 546–549 (2009).
14. B. R. Johnson *et al.*, *Nat. Phys.* **6**, 663–667 (2010).
15. M. Brune *et al.*, *Phys. Rev. Lett.* **77**, 4887–4890 (1996).
16. G. Kirchmair *et al.*, *Nature* **495**, 205–209 (2013).
17. L. Lutterbach, L. Davidovich, *Phys. Rev. Lett.* **78**, 2547–2550 (1997).
18. Z. Leghtas *et al.*, *Phys. Rev. A* **87**, 042315 (2013).
19. W. H. Zurek, *Nature* **412**, 712–717 (2001).
20. C. M. Caves, A. Shaji, *Opt. Commun.* **283**, 695–712 (2010).
21. S. Deléglise *et al.*, *Nature* **455**, 510–514 (2008).
22. A. Ourjoumtsev, H. Jeong, R. Tualle-Brouri, P. Grangier, *Nature* **448**, 784–786 (2007).
23. P. Bertet *et al.*, *Phys. Rev. Lett.* **89**, 200402 (2002).
24. See accompanying supplementary materials for details.
25. M. Boissonneault, J. M. Gambetta, A. Blais, *Phys. Rev. A* **79**, 013819 (2009).
26. H. Paik *et al.*, *Phys. Rev. Lett.* **107**, 240501 (2011).
27. C. Monroe, D. M. Meekhof, B. E. King, D. J. Wineland, *Science* **272**, 1131–1136 (1996).
28. D. I. Schuster *et al.*, *Nature* **445**, 515–518 (2007).
29. S. Haroche, J. M. Raimond, *Exploring the Quantum: Atoms, Cavities, and Photons* (Oxford Univ. Press, Oxford, 2006).
30. S. L. Braunstein, P. van Loock, *Rev. Mod. Phys.* **77**, 513–577 (2005).
31. S. E. Nigg, S. M. Girvin, *Phys. Rev. Lett.* **110**, 243604 (2013).
32. H. Jeong, T. Ralph, *Phys. Rev. A* **76**, 042103 (2007).

Acknowledgments: We thank M. D. Reed, M. Hatridge, and T. L. Brecht for discussions. This research was supported by NSF (grant PHY-0969725), the Office of the Director of National Intelligence (ODNI), the Intelligence Advanced Research Projects Activity (IARPA) through the Army Research Office (W911NF-09-1-0369), and the U.S. Army Research Office (W911NF-09-1-0514). Facilities use was supported by the Yale Institute for Nanoscience and Quantum Engineering (YINQE) and NSF (MRSECDMR 1119826). S.M.G. and Z.L. acknowledge support from NSF (DMR-1004406). M.M. and Z.L. acknowledge support from French Agence Nationale de la Recherche under the project EPOQ2 (ANR-09-JCJC-0070).

Supplementary Materials

www.sciencemag.org/content/342/6158/607/suppl/DC1
Materials and Methods
Supplementary Text
Figs. S1 to S10
Tables S1 and S2
References (*33*–*37*)

16 July 2013; accepted 18 September 2013
Published online 26 September 2013;
10.1126/science.1243289